Measurement Science
and Technology

PURPOSE-LED
PUBLISHING™

PAPER • **OPEN ACCESS**

A 3D adaptive spiral coverage path planning algorithm of autonomous underwater vehicle for enhanced edge-corner coverage

To cite this article: Zhaoye Chen *et al* 2025 *Meas. Sci. Technol.* **36** 076309

View the article online for updates and enhancements.

You may also like

- Thermally-driven large current-perpendicular-to-plane magnetoresistance in ultrathin flakes of vanadium diselenide
  Seyedamin Firouzeh, Md Wazedur Rahman and Sandipan Pramanik
- Effects of the addition of casein phosphopeptide-amorphous calcium phosphate (CPP-ACP) on mechanical properties of luting and lining glass ionomer cement
  Farzin Heravi, Hossein Bagheri, Abdolrasoul Rangrazi et al.
- AUV way-point tracking at constant velocity: cross-track error (CTE) and line-of-sight (LOS) guidance
  Pritam Ghosh and Pranibesh Mandal

This content was downloaded from IP address 182.53.150.215 on 22/06/2026 at 14:58

OPEN ACCESS
IOP Publishing

Measurement Science and Technology

Meas. Sci. Technol. **36** (2025) 076309 (16pp)

https://doi.org/10.1088/1361-6501/ade899

A 3D adaptive spiral coverage path planning algorithm of autonomous underwater vehicle for enhanced edge-corner coverage

Zhaoye Chen[1], **Jiaxin Gao**[2], **Jiahui Ma**[2] **and Xiang Wang**[2,*]

[1] School of Statistics and Mathematics, Central University of Finance and Economics, Beijing 102206, People's Republic of China
[2] College of Engineering, Hebei Normal University, Shijiazhuang 050024, Hebei, People's Republic of China

E-mail: wangxiang@hebtu.edu.cn, 2022310987@email.cufe.edu.cn, gaojiaxin@stu.hebtu.edu.cn and majh@stu.hebtu.edu.cn

Received 28 October 2024, revised 8 March 2025
Accepted for publication 26 June 2025
Published 7 July 2025

Abstract

Underwater acoustic sensor networks (UASNs) are frequently employed in marine engineering, such as ocean data acquisition, marine resource exploration, and undersea disaster prevention. In UASNs, autonomous underwater vehicles (AUVs) are deployed as mobile anchor nodes to assist in locating or communicating with sensor nodes. A major challenge is ensuring that the AUVs path trajectory covers all unknown nodes, especially in edge-corner areas with higher node density due to ocean currents. Traditional coverage path planning algorithms (CPPs) tend to have low coverage in the edge-corner areas, leading to poor localization and communication. This paper proposes the adaptive spiral CPP (AS-CPP) for three-dimensional (3D) marine environments. The AS-CPP uses a spiral model, dynamically adjusting the path's shape and radius based on node density, ensuring higher edge-corner coverage with low energy consumption. The control parameters were identified using shape mapping theory, and the algorithm was validated through MATLAB simulations. Performance metrics such as coverage rate, path smoothness, length, and energy usage were calculated. The results show that AS-CPP has significant advantages over traditional methods such as SCAN, HILBERT, CIRCLES, and SPIRAL, achieving a coverage rate of up to 96% and reducing energy consumption by up to 56%.

Keywords: underwater acoustic sensor networks, autonomous underwater vehicles, coverage path planning, coverage of edges and corners nodes

* Author to whom any correspondence should be addressed.

Original content from this work may be used under the terms of the Creative Commons Attribution 4.0 licence. Any further distribution of this work must maintain attribution to the author(s) and the title of the work, journal citation and DOI.

© 2025 The Author(s). Published by IOP Publishing Ltd

1. Introduction

Autonomous underwater vehicles (AUVs) are capable of navigating underwater target areas independently. Consequently, AUVs are frequently employed in underwater tasks such as ocean monitoring [1, 2], seabed exploration [3, 4], and rescue operations [5, 6]. In particular, AUVs are frequently employed as mobile anchor nodes in underwater acoustic sensor networks (UASNs), by using their communication information at sampling points along their travelling paths to assist sensor nodes and other devices in localization and communication [7, 8]. However, AUVs are constrained by their inability to replenish energy autonomously, which limits their operational time and range. Therefore, effective path planning and obstacle avoidance are crucial for AUVs to safely and accurately complete underwater missions. In recent years, path planning strategies and obstacle avoidance technologies for AUVs have become a hot topic in AUV research. In the field of path planning, researchers classify methods into two main categories [9, 10]: global path planning and local path planning. Global path planning, also known as static path planning, is a technique that relies on the prior knowledge of all static obstacles within a mission area [11, 12]. For global path planning, a range of algorithms have been employed, including the A* algorithm [13], the genetic algorithm [14], the particle swarm optimization algorithm [15], and others. Local path planning, also known as dynamic path planning, is a technique used to deal with unknown or dynamic obstacles within mission area. It is primarily employed when the environment is uncharted or unpredictable. For local path planning, the classical algorithms include rapidly-exploring random trees [16], neural networks [17], and deep reinforcement learning [18].

Although global and local path planning each plays an irreplaceable role, in specific application scenarios, such as marine resource exploration [19], underwater topographic mapping [20], or AUV-aided localization and communication for UASNs [21], the tasks for AUVs not only go beyond simple point-to-point movement but also need to provide comprehensive coverage of the entire mission area without dead corner. Especially in AUV-aided localization and communication for UASN scenarios, the coverage for sensor nodes needs to be considered. Therefore, when planning paths for AUVs supporting the localization of UASNs, in addition to considering the path length and energy consumption, it is crucial to emphasize the coverage of nodes along the path. This study focuses on path planning for scenarios where sensor nodes are irregularly distributed in the mission area, especially in edge-corner dense regions. Accordingly, the focus is on improving the coverage of AUV paths to edge and corner nodes [10].

At present, the most commonly used global path planning curves that take node coverage issues into account are SCAN, HILBERT, CIRCLES, and SPIRAL curves [22]. An illustration of these curves can be found in figure 1. In the SCAN curve, the AUV begins its trajectory in a straight line along the horizontal axis, subsequently changing direction upon reaching the edge of the area. Subsequently, the AUV progresses a specified distance along the vertical axis while continuing to turn along the horizontal axis until the entire target area has been covered. In 2024, Chen *et al* [23] proposed an ant colony path planning optimization based on opposition-based learning to address incomplete coverage and redundant paths in AUV path planning. This was achieved by employing the SCAN curve as a unit cover path to enhance the coverage rate in irregular regions. Nevertheless, when utilizing the SCAN curve for the purpose of localizing UASN'S nodes, it can exhibit considerable covariance issues, which have the potential to affect the success rate and accuracy of node localization, and may also result in redundant coverage.

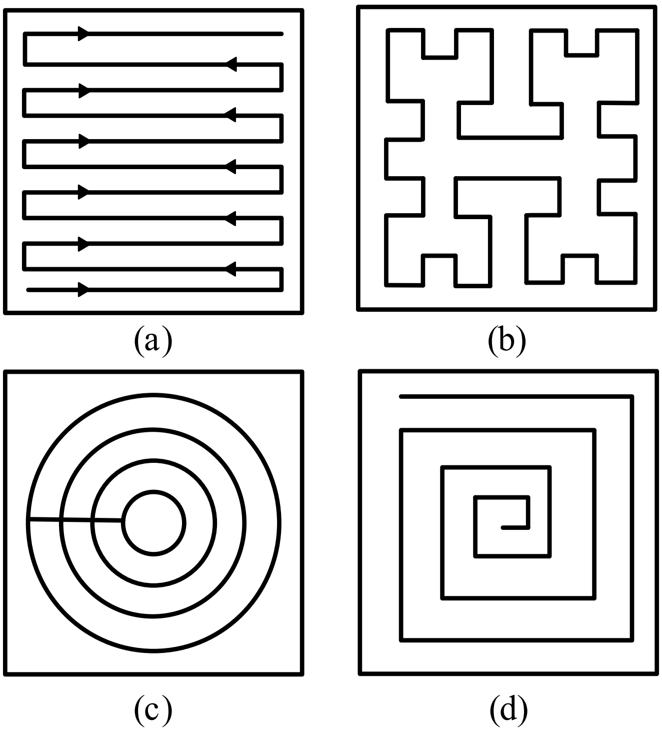

Figure 1. Common coverage path planning curves (a) SCAN; (b) HILBERT; (c) CIRCLES; (d) SPIRAL.

Another frequently utilized coverage path trajectory is the Hilbert curve. It solves the covariance problem in node localization without significantly increasing the path length. In 2020, Fellah and Kechar [24] demonstrated the advantages of HILBERT curves in terms of energy saving, coverage, etc, when compared to curves generated by other optimization methods. Nevertheless, the paths generated by the HILBERT algorithm are unable to provide comprehensive coverage of the mission's edge-corner regions. Consequently, when the AUV traverses the curve, the trajectory does not ensure 100% signal coverage of the nodes situated in these edge-corner areas.

In 2020, Thilagavathi and Manickam [25] conducted a study of the CIRCLES path, noting that it moves along a circular trajectory, thereby reducing issues of broadcast collinearity points. Furthermore, the circular path allows the

AUV to constantly change direction, which minimizes the accumulation of errors resulting from prolonged movement in a single direction. However, when applied to rectangular mission areas, particularly the rectangular corner regions, the CIRCLES curve is unable to effectively cover the area, resulting in unsatisfactory localization outcomes. Therefore, while the 3D spiral curve based on CIRCLES addresses collinearity and accumulated error issues, it is unable to maintain signal coverage in edge-corner areas.

These literatures indicate that both the SCAN and HILBERT algorithms have been extended to 3D curves for implementation in seafloor environments. However, these algorithms are constrained by the inherent characteristics of curves, which result in low smoothness and a high number of turns. Furthermore, they are unable to dynamically adjust their parameters according to the actual situation in the mission area. These issues result in inadequate coverage of the edge-corner region, increased energy consumption, and reduced efficiency of the AUV during its traversal. Additionally, the CIRCLES curve also demonstrates a low level of coverage in the edge-corner task area, resulting in poor accuracy in the localization of underwater sensor nodes assisted by the AUVs.

In addition to SCAN, HILBERT, and CIRCLES curves, Spiral path curves represent another common type of coverage path planning. In 2008, Hu *et al* [26] first proposed the spiral path planning algorithm, which demonstrated a notable reduction in path length and energy consumption compared to the CIRCLES algorithm. In 2019, Lu *et al* [27] introduced a distributed deterministic spiral algorithm to achieve full coverage of target areas in the presence of obstacles. In 2024, Li *et al* [28] proposed a rapid and efficient multi-AUV coverage path planning algorithm (CPP) utilizing improved lawnmower and outer spiral path planning methods, Kalman filter navigation, and path tracking considering ocean currents, combined with fault-tolerant control, to accomplish efficient underwater area coverage search with high robustness. However, these algorithms still lack adequate solutions for low edge-corner region coverage and generate numerous sharp turns that rapidly deplete AUV's energy [29]. The variability of the marine environment and the complexity of sensor localization tasks make it necessary to consider multiple underwater factors when performing AUV-assisted node localization in UASNs, such as ocean currents, node communication range, and sensor node density. These factors can significantly impact localization accuracy. In particular, due to constraints such as ocean depth, seawater density, and specific engineering application scenarios, the distribution and density of sensor nodes often vary considerably. Therefore, how to address the impact of different sensor node densities on localization accuracy and ensure that localization algorithms can adapt to varying node distributions and densities has become a widely discussed research topic. For example, in 2024, Wang *et al* [30] proposed a graph-based multi-objective task allocation and path refinement algorithm for AUV-assisted node localization in UASNs. This algorithm effectively shortens the AUV path length while ensuring node localization accuracy. To address the impact of different sensor node densities, the researchers validated the algorithm in a simulation environment with varying numbers of sensor nodes, and the results demonstrated its effectiveness. In the same year, Huang *et al* proposed an information entropy-based AUV trajectory planning method for node localization [31]. This method models the uncertainty of node positions as information entropy and treats AUV trajectory planning as a process of reducing the overall network entropy using a gridded scenario. Through simulation experiments, the authors verified the effectiveness of this method under different sensor node distributions and densities.

In underwater boundary protection, the edge regions of the area are typically equipped with a higher density of communication nodes to ensure comprehensive coverage and real-time communication for underwater security monitoring. Similarly, in aquaculture, farming areas located at the periphery of the water body lead to higher node densities in the edge-corner regions for effective monitoring of parameters such as water quality, temperature, and salinity. Existing path planning algorithms struggle to effectively address these issues, often leading to poor coverage in edge-corner regions and high energy consumption. To significantly enhance coverage efficiency in the edge-corner regions of 3D marine environments, this paper proposes an adaptive spiral CPP (AS-CPP). The core innovation of the algorithm lies in the combination of dynamic shape mapping and a layered adaptive mechanism, addressing the coverage blind spots and energy consumption issues commonly found in traditional algorithms in underwater environments. First, the two-dimensional shape mapping theory proposed by Fong *et al* [32] is extended to 3D space. By introducing the 3D variable rounded square spiral path (3D-VRSSP), the algorithm dynamically transforms static circular spirals into spiral paths that adapt to the distribution of sensor nodes, improving coverage. Second, a dynamic layered strategy based on node density is proposed, where the path pattern is dynamically selected according to the density variance at the edge of each layer. This approach enables shorter paths and lower energy consumption during AUV path planning.

The definitions of the symbols used in this study are provided in table 1. The remainder of this paper is organized as follows. Section 2 introduces the 3D square-circle spiral model and shape mapping theory. Section 3 presents the 3D variable square-circle spiral path planning algorithm and theoretically analyzes path curvature, smoothness, length, coverage, and energy consumption. Finally, section 4 validates the path's feasibility through simulations, compares it with SCAN, Hilbert, CIRCLES, and Spiral algorithms, and discusses the results. The final experimental results demonstrate the algorithm's excellence in positioning coverage, energy consumption, path length, and accuracy.

Table 1. List of notations and corresponding definitions.

Symbol	Definition
h	The pitch of the helix
r	The radius of the 'rounded square'
S_i	The area of the projection of the edge-corner region of layer i
ρ_i	Edge-corner region node density for layer i
n_i	The number of nodes in the edge-corner region between layers i and $i+1$
$\bar{\rho}$	The average node density
ρ_i^{nor}	The normalized node density for layer i
$\bar{\rho}^{\mathrm{nor}}$	The normalized average node density
s_ρ^2	Node density variance
κ	Path smoothness
E	The total energy consumption rate of the AUV

2. Related works

In order to achieve optimal node coverage in target marine areas with high edge-corner region node density, and thus support subsequent tasks such as high-precision node localization and communication, AUVs require efficient navigation paths. Effective path planning is crucial for AUVs to efficiently cover nodes and complete underwater tasks successfully. Major evaluation metrics of the CPP include node coverage rate, path smoothness, path length, and energy consumption. In response, this paper presents the AS-CPP algorithm, which employs a 3D cylindrical spiral model tailored for 3D network environments with high node density in edge-corner regions.

2.1. 3D cylindrical spiral path

The 3D cylindrical spiral model, also referred to as a helical or spiral curve, represents a path that rotates around a central axis while simultaneously moving axially in 3D space. This model is widely observed in both natural and engineering applications, including the structures of DNA, spiral staircases, and screws.

Consider an underwater 3D rectangular task area with a base edge length of 2 l and a height of H. In the 3D cylindrical spiral path, let r denote the spiral radius and t the AUV's travel time. The expression for any point $A(x_a, y_a, z_a)$ on the 3D cylindrical spiral path is given by:

$$\begin{cases} x_a = r\cos(\omega t) \\ y_a = r\sin(\omega t) \\ z_a = v_z t \end{cases} \tag{1}$$

where ω represents the angular velocity, indicating the rate of rotation of the AUV around the cylindrical axis, its relation to the rotation angle θ is given by $\theta = \omega t$. The linear velocity v_z represents the AUV's vertical speed along the cylindrical axis (z-direction) and thus determines the spiral's rate of height change.

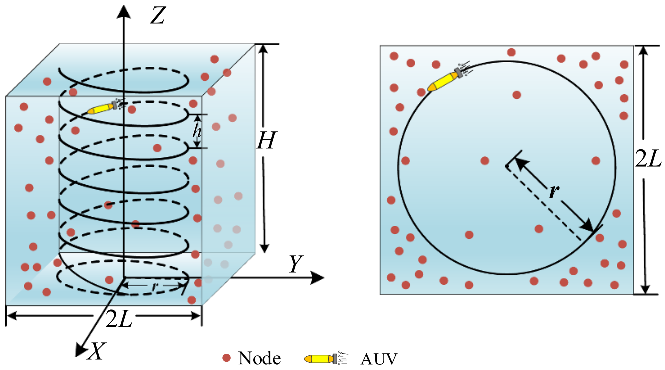

Figure 2. Schematic diagram of AUV's 3D cylindrical spiral path model. (a) Path plan view; (b) path top view.

From equation (1), the pitch h of the helix is:

$$h = v_z \frac{2\pi}{\omega}. \tag{2}$$

By adjusting the parameters, various types of spirals, such as conical spirals, can be obtained. Using a 3D cylindrical spiral trajectory for AUV motion may lead to coverage blind spots in the mission area. This study addresses this issue by using shape mapping and node density in the edge-corner region to adjust the parameters.

Figures 2(a) and (b) show the plan and top views of the 3D cylindrical spiral path, respectively. As shown in figure 2, within a 3D underwater network, the AUV moves along the spiral path and communicates with target nodes. By adjusting the spiral's roundness to bring the path closer to edge-corner region nodes, node coverage can be effectively enhanced, thereby improving subsequent tasks such as node localization, tracking, and navigation.

2.2. Shape mapping theory

Salgar *et al* proposed a shape mapping theory centered on radial mapping, which transforms a circle into a rounded square or a square [22]. In the two-dimensional plane XOY, let N be any point on the X-axis. The point $A(x_a, y_a)$ is mapped to point $B(x_a, y_a)$ via a constraint function, satisfying $\angle AON = \angle BON$.

As shown in figure 3, radial mapping allows point A on a circle with radius r to be mapped along the radial line (the circle's radius direction OA) from the center O to point B, achieving the shape transformation.

Figure 3 demonstrates the mapping process from a circle to a 'rounded square,' which is between a square and a circle. Let r represent the radius of the 'rounded square.' The radial mapping of point A to point B is constrained by the following equations:

$$\begin{cases} x_b = x_a \times (1 - \rho \times (1 - |x_a|/r)) \\ y_b = y_a \times (1 - \rho \times (1 - |y_a|/r)) \end{cases} \tag{3}$$

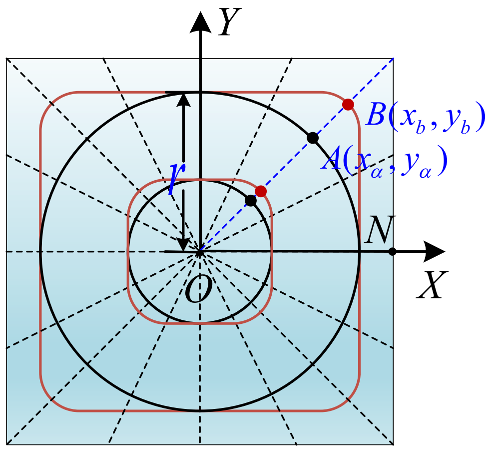

Figure 3. Schematic diagram of radial mapping from a circle to a rounded square.

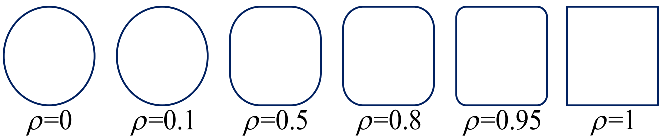

Figure 4. Schematic diagrams of the degree of mapping.

where ρ is a parameter between 0 and 1. When $\rho = 0$, the mapping results in a circle; when $\rho = 1$, the shape approaches a square (though with rounded corners). For $0 < \rho < 1$, the result is a rounded square shape between a circle and a square.

As shown in equation (3), points on the original circle near the task area's edges and corners undergo minor changes, while points farther from the edges and corners are 'pushed' outward along the radial direction to be closer to the square's edges and corners, reducing the distance to the task area edges and corners. As shown in figure 4, ρ controls the degree of 'squaring'; the closer ρ is to 1, the more the shape resembles a square. But each value of can create a smooth shape mapping.

This study intends to apply the shape mapping theory by adjusting parameters to transform the circular cross-section of the 3D cylindrical spiral model into a rounded square that adapts to the task area's layered node density. This will increase the coverage area of communication signals to the edge and corner areas during AUV movement. Figures 5(a) and (b) show the plan view and top view of the 3D cylindrical spiral path, respectively.

3. 3D AS-CPP

3.1. Delineation of layered edge-corner region and definition of node density

The task area should be layered and the degree of squaring and rounded square radius of the spiral path mapped on each layer determined based on the node density in the edge-corner

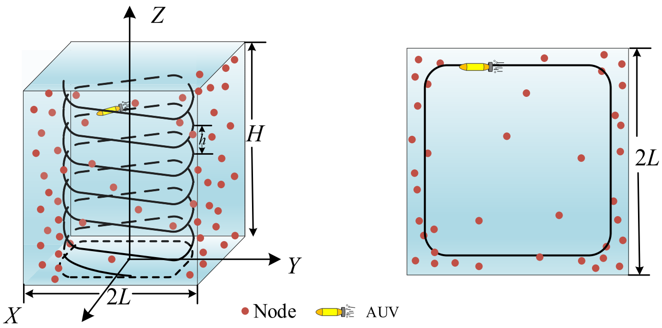

Figure 5. Schematic diagram of the AUV's 3D rounded square spiral path model. (a) Path plan view; (b) path top view.

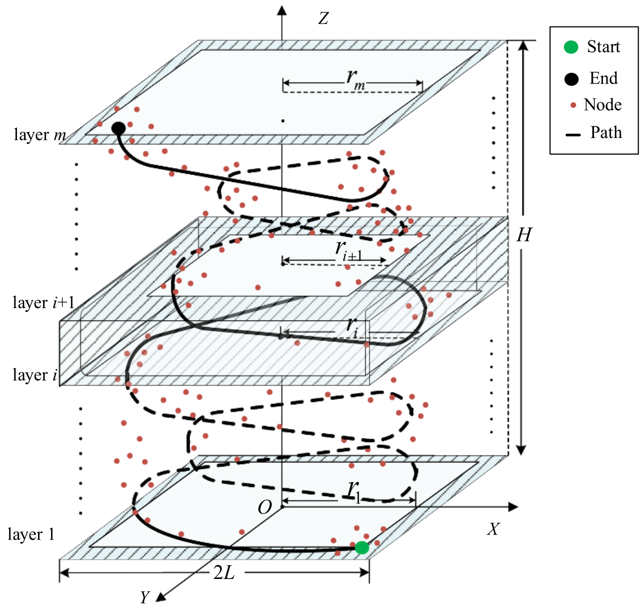

Figure 6. Schematic diagram of AS-CPP layering and edge-corner region.

regions of each layer. It is assumed that the task area is a cuboid with a base edge length of $2L$ and a height of H, divided uniformly into m layers. In this study, the edge-corner region of the ith layer is defined as the 3D area between the ith and $i+1$th layer ($i = 1, 2, \ldots, m$), as shown in figure 6.

As shown in figure 6, the radius of the variable rounded square is dynamically adjusted based on the node density in the edge-corner region, forming a 3D-VRSSP. Subsequently, the path coverage is analyzed from the perspective of the *XOY* plane projection of the edge region. Figure 7 shows the projection of the path planning for an AUV following a 3D cylindrical spiral (dashed circle) and the proposed 3D-VRSSP (solid rounded square). The shaded area in figure 7 represents the projection of the 3D edge-corner region. When the node density in the edge-corner region is high, the AS-CPP path significantly enhances node coverage.

In figure 7, when $r_i \neq r_{i+1}$, meaning that there is inequality in the radii of the squares of the two neighboring layers,

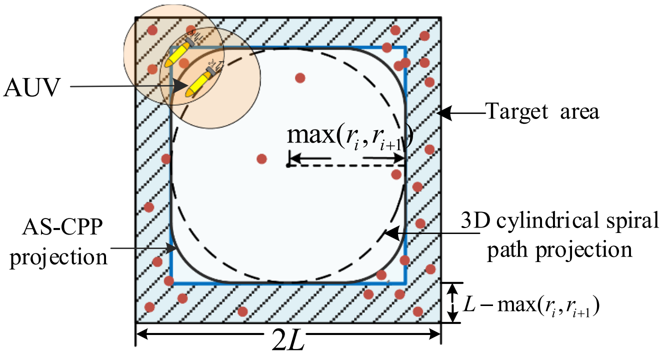

Figure 7. Schematic projection of the edge-corner region of layer *i*.

the edge-corner region is determined by the larger radius, as shown by the blue solid squares in figure 7. Consequently, the area of the projection S_i of the edge-corner region of layer i can be expressed as follows:

$$S_i = (L - \max(r_i, r_{i+1})) \times 2L \times 4 - 4(L - \max(r_i, r_{i+1}))^2. \tag{4}$$

In order to provide further analysis of the algorithm, three parameters are defined: edge-corner region node density, average node density, and normalized average node density.

Definition 1: The spiral radii of layers i and $i+1$ ($I = 1, 2, \ldots, m$) are defined as r_i, r_{i+1}, respectively. The number of nodes in the edge-corner region between layers i and $i+1$ is n_i. The edge-corner region node density ρ_i for layer i is defined as follows:

$$\rho_i = \frac{n_i}{S_i}. \tag{5}$$

The average node density $\bar{\rho}$ across the m layers of the task area's edge-corner regions is given by the following equation:

$$\bar{\rho} = \frac{1}{m}\sum_{i=1}^{m} \rho_i. \tag{6}$$

The normalized node density ρ_i^{nor} for layer i and the normalized average node density $\bar{\rho}^{\mathrm{nor}}$ for the task area is given by the following equations:

$$\rho_i^{\mathrm{nor}} = \frac{\rho_i - \rho_{\min}}{\rho_{\max} - \rho_{\min}} \tag{7}$$

$$\bar{\rho}^{\mathrm{nor}} = \frac{\bar{\rho} - \rho_{\min}}{\rho_{\max} - \rho_{\min}} \tag{8}$$

where $\rho_{\min}, \rho_{\max}$ are the minimum and maximum node density values across all layers. It can be observed from equations (7) and (8) that $0 \leq \rho_i^{\mathrm{nor}}, \bar{\rho}^{\mathrm{nor}} \leq 1$.

3.2. Design of the AS-CPP

To optimize global path planning for better node coverage in the task area, we propose an AS-CPP strategy. The AS-CPP algorithm can design the trajectories based on node distribution patterns, as follows:

1. When variations in edge-corner region node density across layers are minor, a 3D rounded square spiral path is used, reducing algorithmic complexity and computational resources.
2. When there are significant variations, a 3D-VRSSP is employed. Node density variance measures these variations, and although this approach demands more computational resources, it significantly improves the edge-corner node coverage.

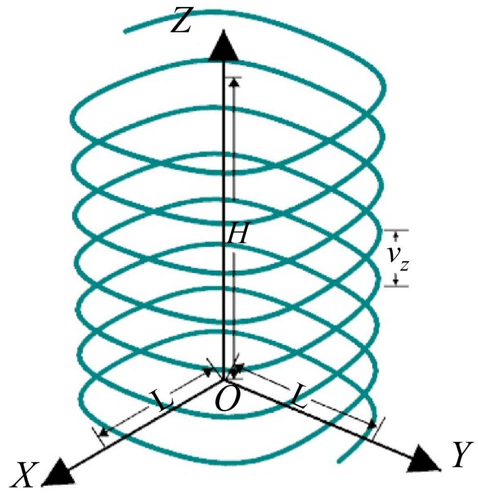

Figure 8. Schematic diagram of three-dimensional rounded square paths.

For the first case, the 3D rounded square spiral path refers to a cylindrical spiral with a fixed rounded square radius (see figure 8). Shape mapping theory is applied to transform the circular spiral into a rounded square shape suited to the task area. The shape is controlled using the normalized average node density $\bar{\rho}^{\mathrm{nor}}$. Let θ be an angle parameter in the range $[0, 2\pi]$, and r be the spiral radius. For any point $B(x_b, y_b, z_b)$ on the 3D rounded square spiral path, we have:

$$\begin{cases} x_b = (r + \bar{\rho}^{\mathrm{nor}} \times \cos(\theta)) \times \cos(\omega t) \\ y_b = (r + \bar{\rho}^{\mathrm{nor}} \times \cos(\theta)) \times \sin(\omega t) \\ z_b = v_z t \end{cases} \tag{9}$$

where $\bar{\rho}^{\mathrm{nor}}$ controls the shape ($\bar{\rho}^{\mathrm{nor}} = 0$ for a circle, $\bar{\rho}^{\mathrm{nor}} > 0$ for a rounded square, and $\bar{\rho}^{\mathrm{nor}} = 1$ approaches a square). By adjusting the curve parameters in equation (9), the spiral's shape and the extent of rounding can be modified. As t increases from 0, point (x_b, y_b, z_b) ascends along the spiral, forming a rounded square projection in the XOY plane, as shown in figure 8.

To more effectively control the degree of 'squaring' during radial mapping, a detailed analysis of the critical control parameter, the normalized mean node density $\bar{\rho}^{\mathrm{nor}}$ is conducted.

Definition 2: Let ρ_i be the node density of the edge-corner region in layer i ($i = 1, 2,\ldots, m$). The node density variance s_ρ^2 is defined as:

$$s_\rho^2 = \frac{1}{m-1}\sum_{i=1}^{m}(\rho_i - \bar{\rho})^2 \tag{10}$$

where $\bar{\rho}$ is the average node density.

1. Baseline determination

In practical applications, a baseline value for the node density variance s_ρ^2 can be obtained through historical data analysis or simulation under normal or ideal conditions. When $s_\rho^2 \geq \bar{s}_\rho^2$, a 3D-VRSSP is selected; otherwise, a 3D rounded square spiral path is used.

2. Threshold range setting

It is recommended that upper and lower thresholds be set to create an acceptable range, with the baseline $\pm\psi$ as the initial threshold range. When $s_\rho^2 \in [\bar{s}_\rho^2 \times (1-\psi), \bar{s}_\rho^2 \times (1+\psi)]$, a 3D rounded square spiral path is selected; otherwise, the VRSSP is employed, where ψ is a variable that can be adjusted according to specific requirements.

Thresholds can be dynamically adjusted based on real-time operations. Frequent threshold triggers necessitate widening the range. The setting of threshold needs to be combined with specific application scenarios and continuously optimized through practice. That is to say, the threshold should be based on the actual needs and performance goals of the system, such as combining multi-objective optimization to comprehensively set the weights of node coverage, path length, node coverage, energy consumption, etc. to set the threshold.

For the second case, the 3D-VRSSP involves a spiral with a variable radius and 'squaring' degree that enhances node coverage in edge-corner regions. The radius of the rounded square projection is dynamically adjusted based on each layer's node density.

When the node density variance $s_{\rho_i}^2$ is large, indicating significant differences between layers ($s_\rho^2 \gg \bar{s}_\rho^2$), the spiral radius is modified to create a 3D rounded square spiral with a variable cross-section radius, as shown in figure 9. The radius of the rounded square is controlled using the normalized node density $\bar{\rho}_i^{\text{nor}}$ ($i = 1, 2,\ldots, m$)for each layer.

Furthermore, the parametric equations for the 3D-VRSSP are provided. Let θ be the angle parameter in the range $[0, 2\pi]$ and $\theta = \omega t$. For any point $B'(x_{ib}, y_{ib}, z_{ib})$ on the path in layer i, the following equation applies:

$$\begin{cases} x_{ib} = \rho_i^{\text{nor}} \times \left(1 - \bar{\rho}_i^{\text{nor}} + \bar{\rho}_i^{\text{nor}} \times \frac{\sqrt{2}}{2} \times (\cos(\theta) + \sin(\theta))\right) + L \\ y_{ib} = \rho_i^{\text{nor}} \times \left(1 - \bar{\rho}_i^{\text{nor}} + \bar{\rho}_i^{\text{nor}} \times \frac{\sqrt{2}}{2} \times (\cos(\theta) - \sin(\theta))\right) + L \\ z_{ib} = v_z t \end{cases} . \tag{11}$$

The introduction of the variable radius parameter $\bar{\rho}_i^{\text{nor}}$ to replace the fixed radius parameter r enables the radius to adapt in accordance with the density of nodes in each layer as the path progresses. This results in the formation of a self-adjusting spiral that expands or contracts over time t.

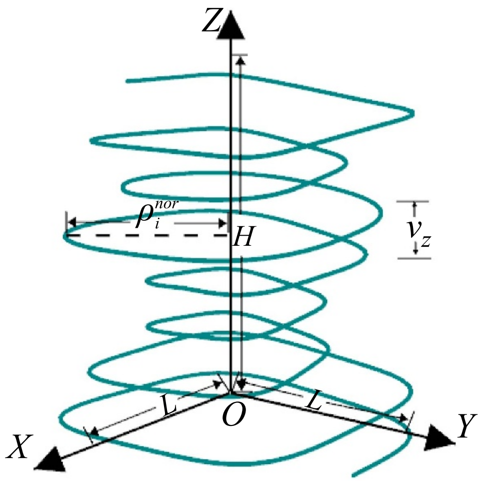

Figure 9. Schematic diagram of three-dimensional variable rounded square paths.

The degree of 'squaring' is controlled by $\bar{\rho}_i^{\text{nor}}$, which allows the curve to transition smoothly between square and circular shapes as shown in equation (11). When $\bar{\rho}_i^{\text{nor}} = 0$, the projection is a perfect circle; when $\bar{\rho}_i^{\text{nor}} = 1$, it is a smooth square; when the value of $\bar{\rho}_i^{\text{nor}}$ varies between 0 and 1, the projected surface smoothly transitions from circle to square.

If $R(t)$ denotes the variable radius function, it can be expanded as follows:

1. Linear variation: $R(t) = R(0) + kt$ (where $R(0)$ is the initial radius, k is the rate of change).
2. Periodic variation: $R(t) = R(0) + A\sin\omega t$ (where $R(0)$ is the average radius, A is the amplitude, ω is the angular frequency).
3. Exponential variation: $R(t) = R(0)\,e^{kt}$ (where $R(0)$ is the initial radius, k is the growth rate);

Moreover, if $v_z(t)$ represents the ascending height of the 3D-VRSSP at time t, in addition to in $v_z(t) = v_z t$ equation (11), $v_z(t)$ can also be replaced by the following function, allowing the pitch of the helical curve to vary more flexibly with t:

1. Linear variation: $v_z(t) = bt$.
2. Quadratic function: $v_z(t) = bt^2$ (slow rise initially, accelerating later).
3. Sine variation: $v_z(t) = b(1-\cos(\pi t))/2$ (slow at start and end, fast in the middle).
4. Exponential variation: $v_z(t) = b(e^{kt}-1)/(e^{kt}-1)$ (controlled by k; faster growth with $k > 0$, slower start with $k < 0$).

3.3. Path performance evaluation

For coverage paths, the path coverage rate and path energy consumption are two critical factors for evaluating path planning efficiency. Typically, path energy consumption is closely related to path smoothness and path length. Greater path smoothness generally results in lower energy consumption, while greater path length tends to increase energy consumption, and vice versa. Therefore, to evaluate the energy consumption of AS-CPP, it is essential to analyze and calculate its smoothness and path length.

Firstly, the smoothness of AS-CPP is analyzed. For coverage paths, a lower curvature indicates a smoother path. Alternatively, a smaller change in the angle between tangent directions at adjacent points implies a smoother path, which in turn leads to reduced energy consumption [10]. However, calculating changes in adjacent tangent angles requires real-time path sampling and is computationally intensive. Therefore, the definition of path curvature is introduced in order to quantify the smoothness of the AS-CPP path.

Definition 3: The path curvature $\kappa_{r(t)}$ at the position vector $r(t)$ of a 3D curve is defined as follows:

$$\kappa_{r(t)} = |r'(t) \times r''(t)| / |r'(t)|^3 \tag{12}$$

where $r'(t)$ is the velocity vector, $r''(t)$ is the acceleration vector, and denotes the cross product.

In practical applications, additional factors such as curvature continuity and acceleration continuity must be considered to comprehensively evaluate path smoothness. Based on the definition of path curvature, we further define the smoothness of the trajectory path.

Definition 4: Let $\kappa_{r(t)}$ be the path curvature at the position vector $r(t)$ on the curve, and L is the total path length. Path smoothness κ is defined as:

$$\kappa = 1 / \left(1 + \frac{\int \kappa_{r(t)} \mathrm{d}r(t)}{L}\right). \tag{13}$$

To compare the path curvature of the 3D rounded square spiral path and the 3D-VRSSP in AS-CPP, we propose theorem 1.

Theorem 1. *The path curvature of a standard 3D cylindrical spiral path is* $\frac{\sqrt{{v_z}^2 r^2 \omega^4 \sin^2(\omega t) + r^4 \omega^6}}{(r^2\omega^2 + {v_z}^2)^{\frac{3}{2}}}$, *and the path curvature of a 3D rounded square path is* $\frac{(r+\bar{\rho}_i^{\mathrm{nor}}\cos\theta)\omega^2\sqrt{v^2+(r+\bar{\rho}_i^{\mathrm{nor}}\cos\theta)^2\omega^4}}{\left[(r+\bar{\rho}_i^{\mathrm{nor}}\cos\theta)^2\omega^2+v^2\right]^{\frac{3}{2}}}$.

Proof of Theorem 1. (1) For the standard 3D cylindrical spiral path, calculate the position vectors $r'(t)$ and $r''(t)$ from equation (1):

$$r'(t) = (-r\omega \sin(\omega t), r\omega \cos(\omega t), v_z) \tag{14}$$

$$r''(t) = \left(-r\omega^2 \cos t, r\omega^2 \sin t, 0\right). \tag{15}$$

Calculate the cross product and magnitude:

$$|r'(t) \times r''(t)| = \sqrt{{v_z}^2 r^2 \omega^4 \sin^2(\omega t) + r^4 \omega^6} \tag{16}$$

$$|r'(t)|^3 = \left(r^2\omega^2 + {v_z}^2\right)^{\frac{3}{2}}. \tag{17}$$

Therefore, calculate the curvature at the position vector $r(t)$ from equation (18):

$$\kappa_{r(t)} = \frac{\sqrt{{v_z}^2 r^2 \omega^4 \sin^2(\omega t) + r^4 \omega^6}}{(r^2\omega^2 + {v_z}^2)^{\frac{3}{2}}} \tag{18}$$

(2) For the 3D rounded square path, if the position vector $r(t) = (x, y, z)$ is at the ith layer:

The first derivative can be expressed as follows:

$$x' = -\left(r + \bar{\rho}_i^{\mathrm{nor}} \cos\theta\right) \omega^2 \sin \omega t \tag{19}$$

$$y' = -\left(r + \bar{\rho}_i^{\mathrm{nor}} \cos\theta\right) \omega^2 \cos \omega t \tag{20}$$

$$z' = v_z. \tag{21}$$

And the second derivative can be expressed as follows:

$$x'' = -\left(r + \bar{\rho}_i^{\mathrm{nor}} \cos\theta\right) \omega^2 \cos \omega t \tag{22}$$

$$y'' = -\left(r + \bar{\rho}_i^{\mathrm{nor}} \cos\theta\right) \omega^2 \sin \omega t \tag{23}$$

$$z'' = 0. \tag{24}$$

Then the path curvature at position vector $r(t)$ is calculated from equation (25) as.

$$\kappa_{r(t)} = \frac{\sqrt{(z''y' - y''z')^2 + (x''z' - z''x')^2 + (y''x' - x''y')^2}}{\left(x'^2 + y'^2 + z'^2\right)^{\frac{3}{2}}}. \tag{25}$$

Substituting equations (19)–(24) into equation (25), the final curvature at $r(t) = (x, y, z)$ can be denoted as:

$$\kappa_{r(t)} = \frac{(r + \bar{\rho}_i^{\mathrm{nor}} \cos\theta)\omega^2 \sqrt{v^2 + (r + \bar{\rho}_i^{\mathrm{nor}} \cos\theta)^2 \omega^4}}{\left[(r + \bar{\rho}_i^{\mathrm{nor}} \cos\theta)^2 \omega^2 + v^2\right]^{\frac{3}{2}}} \tag{26}$$

(3) For the 3D-VRSSP, if the position vector $r(t) = (x_i, y_i, z_i)$ is located at the ith layer, the first step is to calculate the derivatives:

$$x_i' = \rho' \sqrt{(1 - \rho^2)} + \frac{\rho(-\rho\rho')}{\sqrt{(1 - \rho^2)}} \tag{27}$$

$$y'_i = \rho' \sqrt{(1 - \rho^2)} + \frac{\rho(-\rho\rho')}{\sqrt{(1 - \rho^2)}}. \tag{28}$$

Derive the expressions for x_i'' and y_i'' from equations (27) and (28) and substitute them into the curvature equation (25).

$$\kappa_{r(t)} = \frac{|x'y'' - y'x''|}{(x^2 + y^2)^{\frac{3}{2}}}. \tag{29}$$

The expressions for x_i and y_i are similar, which may simplify the final curvature expression. Additional normalization function ρ_i^{nor} information for each layer's node density can further simplify the results. □

A further analysis of the relationship between energy consumption and path smoothness in AS-CPP is conducted based on the curvature calculation. The path smoothness is defined as a comprehensive measure of curvature across the entire path. The relationship between path smoothness and energy consumption is then analyzed, resulting in the formulation of definition 5 and theorem 2.

Definition 5. Let v be the AUV's speed, and κ represent path smoothness. Then the total energy consumption rate E of the AUV is given by [23]:

$$E = k_1 \times v^2 + k_2 \times \kappa^{-2} \times v^2 \tag{30}$$

where k_1 and k_2 are constant coefficients.

It can be demonstrated that greater path smoothness κ results in lower energy consumption E. Furthermore, it can be shown that the impact of κ on energy consumption is more significant when the speed v is faster. The term $k_1 \times v^2$ represents the baseline energy consumption for linear motion, while $k_2 \times \kappa^{-2} \times v^2$ represents the additional energy due to turns. It should be noted that the actual model may be more complex, taking into account factors such as currents and drag.

Theorem 2. *Let κ denote path smoothness. When path length and AUV speed remain constant, the total energy consumption rate E of the AUV is inversely proportional to κ^2.*

Proof of Theorem 2. In this analysis, the energy consumption of the other AUV components is ignored; instead, the focus is on two key factors [23] that contribute primarily to the overall energy usage. The first of these factors is the energy consumed by the AUV as it travels through its operational environment. The second factor is the energy consumed by the AUV in maintaining a hovering position while receiving data. It is important to note that the latter factor is relatively minor and can be considered negligible.

Assuming the AUV travels at a constant speed throughout, from equation (30), the total energy consumption rate E usually consists of two components: linear motion energy consumption rate (related to speed) and turning energy consumption rate (related to curvature). Since v is constant, the term $k_1 \times v^2$ is also constant, showing that E is inversely proportional to κ^2.

Thus, when the path length and the operating speed of the AUV remain unchanged, the total energy consumption rate is inversely proportional to the square of the path smoothness. □

This section defines the path energy consumption rate and proves that greater path smoothness results in a reduction in the energy consumption of the AUV.

Additionally, a computational analysis of the path length for the coverage algorithm is conducted. Calculating the path length requires the arc length formula for parametric curves. First, compute $\frac{\mathrm{d}x}{\mathrm{d}t}$, $\frac{\mathrm{d}y}{\mathrm{d}t}$ and $\frac{\mathrm{d}z}{\mathrm{d}t}$, calculated results are shown in equation (31). The 3D rounded square spiral path, after shape mapping, has a projection with a fixed radius between a circle and a square,

$$\begin{cases} \frac{\mathrm{d}x_b}{\mathrm{d}t} = -\left(r + \left(\bar{\rho}_i^{\mathrm{nor}}\right) \hat{}\ \sec \times \cos(\theta)\right) \times \sin(\omega t) \\ \frac{\mathrm{d}y_b}{\mathrm{d}t} = \left(r + \left(\bar{\rho}_i^{\mathrm{nor}}\right) \hat{}\ \sec \times \cos(\theta)\right) \times \cos(\omega t) \\ \frac{\mathrm{d}z_b}{\mathrm{d}t} = v_z \end{cases} . \tag{31}$$

The arc length is calculated as:

$$L = \int \sqrt{\left[\left(\frac{\mathrm{d}x_b}{\mathrm{d}t}\right)^2 + \left(\frac{\mathrm{d}y_b}{\mathrm{d}t}\right)^2 + \left(\frac{\mathrm{d}z_b}{\mathrm{d}t}\right)^2\right]}\,\mathrm{d}t. \tag{32}$$

Substitution of equation (31) into equation (32), with the objective of simplifying the equation, gives rise to the following result:

$$L = \int \left[\left(r + \left(\bar{\rho}_i^{nor}\right)^{\sec\cos(\theta)}\right)^2 + {v_z}^2\right]^{\frac{1}{2}} \mathrm{d}t. \tag{33}$$

As both $(r + (\bar{\rho}_i^{\mathrm{nor}})^{\sec \times \cos(\theta)})^2$ and ${v_z}^2$ are constants, they can be factored out of the integral.

$$L = \left[\left(r + \left(\bar{\rho}_i^{\mathrm{nor}}\right)^{\sec\cos(\theta)}\right)^2 + {v_z}^2\right]^{\frac{1}{2}} \int \mathrm{d}t. \tag{34}$$

Assuming t varies from 0 to T, then:

$$L = \left[\left(r + \left(\bar{\rho}_i^{\mathrm{nor}}\right)^{\sec \times \cos(\theta)}\right)^2 + {v_z}^2\right]^{\frac{1}{2}} T. \tag{35}$$

Let L' be the length of the standard 3D cylindrical spiral path. The path length can be calculated as follows:

$$L' = \left[\left(r^2 + {v_z}^2\right]^{\frac{1}{2}} T. \tag{36}$$

Given that $(r + (\bar{\rho}_i^{\mathrm{nor}})^{\sec \times \cos(\theta)})^2 \geq r^2$, it follows that $L \geq L'$. Furthermore, the length of the 3D rounded square spiral path is dependent on the value of θ. The value of θ serves to increase the complexity of the path shape. However, in general, the length of the 3D rounded square spiral path is greater than that of the standard 3D cylindrical spiral path.

In the case of the 3D-VRSSP, the path length calculation is more complex due to the variation in the rounded square radius in real-time, correlated with the node density of each layer, involving variations in ρ_i^{nor} and θ.

A further crucial metric for coverage paths is the coverage rate. This study is concerned with the analysis of edge-corner coverage rates. The term 'edge-corner region' is used to describe a rectangular annular area with a longitudinal length of $2L$ and a distance from the edge of the task area of (L–R).

In this paper, we define the node coverage rate of the task area as K and the edge-corner region coverage rate as k ($0 < k < 1$), with an average node density of $\bar{\rho}$. We proceed to analyze the relationships among these three parameters.

Theorem 3. *Let n be the total number of nodes in the task area, the volume of the edge-corner region be V^{corner}, and the volume of the central (non-corner) region be V^{center}. Let the number of nodes in the edge-corner region be n^{corner}, and the number of nodes in the non-corner region be n^{center}. When the edge-corner region coverage rate k keeps constant and $r < L$ (including $r \leqslant L$), K is inversely proportional to $\bar{\rho}$ (if $r > L$, the spiral radius r exceeds the baseline length of the target area and is impractical). When the average node density $\bar{\rho}$ remains constant, and K is directly proportional to k.*

Proof of Theorem 3. Start by calculating:

$$V^{\text{corner}} = \left[(2L)^2 - (2r)^2\right] \times 2L = 8L\left(L^2 - r^2\right) \tag{37}$$

$$V^{\text{center}} = (2r)^2 \times 2L = 8r^2 L \tag{38}$$

$$n^{\text{corner}} = \bar{\rho} V^{\text{corner}} = \bar{\rho} \times 8L\left(L^2 - r^2\right). \tag{39}$$

Assuming that the spiral path completely covers the nodes in the central region and partially covers the nodes in the edge-corner region, calculate the number of nodes covered by the spiral path:

$$n^{\text{cover}} = n^{\text{center}} + kn^{\text{corner}} = n - n^{\text{corner}} + kn^{\text{corner}}. \tag{40}$$

Thus, the node coverage rate K for the task area is:

$$K = \frac{n^{\text{cover}}}{n} \times 100\%. \tag{41}$$

The equations (37)–(40) are solved as follows:

$$K = 1 - \frac{\bar{\rho} \times (1-k) \times 8L\left(L^2 - r^2\right)}{n} \times 100\%. \tag{42}$$

From this equation, it is evident that when k remains constant and $r < L$, K is inversely proportional to $\bar{\rho}$. When the average node density $\bar{\rho}$ remains constant, K is directly proportional to k. □

The model in theorem 3 assumes nodes are randomly and uniformly distributed within the area, which may differ in real scenarios. Additionally, specific parameters of the spiral path (such as radius and pitch) and factors like signal attenuation can influence actual coverage, particularly in edge-corner regions.

4. Simulation results and analysis

In this study, the experimental environment was configured using the Windows 11 operating system, a central processing unit operating at 1.60 GHz, and 8 GB of memory. The simulation software employed was MATLAB R2017b, with the simulation parameters detailed in table 2. Based on the approach of Wang *et al* [30], the number of nodes in our study was set between 80 and 140, with the communication radius configured from 300 m to 450 m and the edge-corner node density varied from 30% to 100% to evaluate the performance of the proposed algorithm under different edge-corner density conditions. Additionally, to simulate the practical applicability of our algorithm in real-world environments, we adopted the parameters of the Bluefin-21 AUV according to the experimental conditions for the simulation experiments [33]. Each simulation scenario was executed 1000 times to ensure the robustness and reliability of the results. Figure 10 shows the configuration of the task area, which was arranged with 140 sensor nodes in a square area with dimensions of 1000 m × 1000 m and a depth of 2000 m. The distribution of sensor nodes reflects the task's characteristic of higher density in edge-corner regions.

Table 2. Simulation parameters.

Parameter	Values
Task area	1000 m ×1000 m ×2000 m
Number of nodes	80–140
Edge-corner node density	30%–100%
AUV cross-sectional area	0.026 129 m^2
AUV's communication radius	300 m–450 m
AUV's speed	1 m s^{-1}
Number of simulations	1000

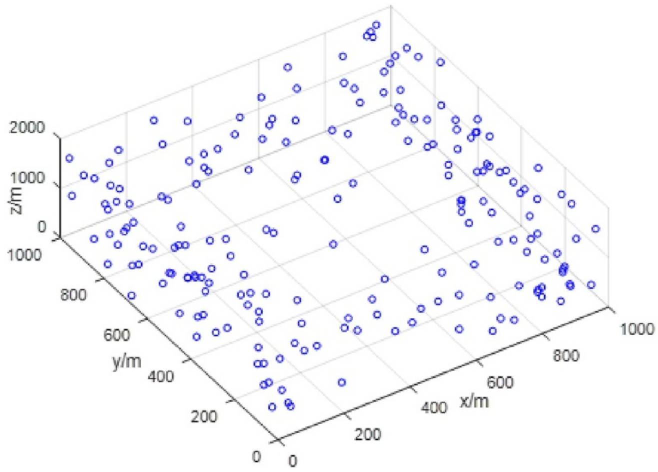

Figure 10. Task area setup map.

The AS-CPP algorithm was evaluated based on five parameters: edge-corner coverage rate, path length, path smoothness, energy consumption, and the accuracy of node localization. Additionally, it was compared with four representative algorithms: SCAN, HILBERT, SPIRAL, and CIRCLES.

4.1. Comparison of coverage rates among algorithms

To investigate the impact of different factors on edge-corner coverage, four variables were considered: number of nodes, edge-corner node density, path sampling point density and communication radius.

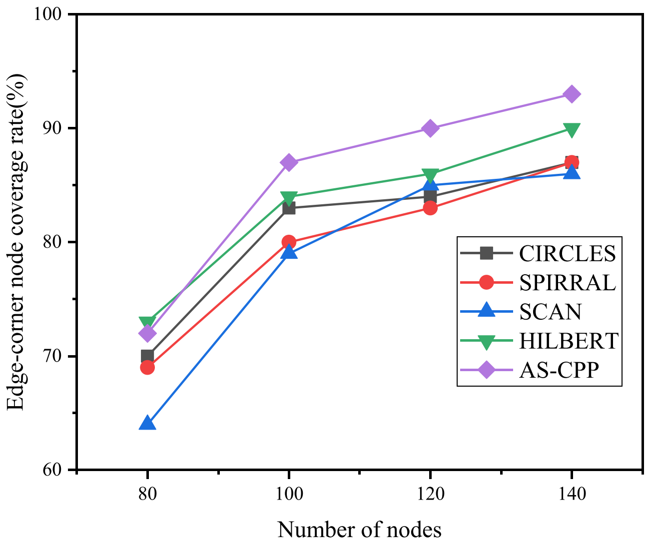

Figure 11. Comparison of edge-corner coverage rates with varying node numbers.

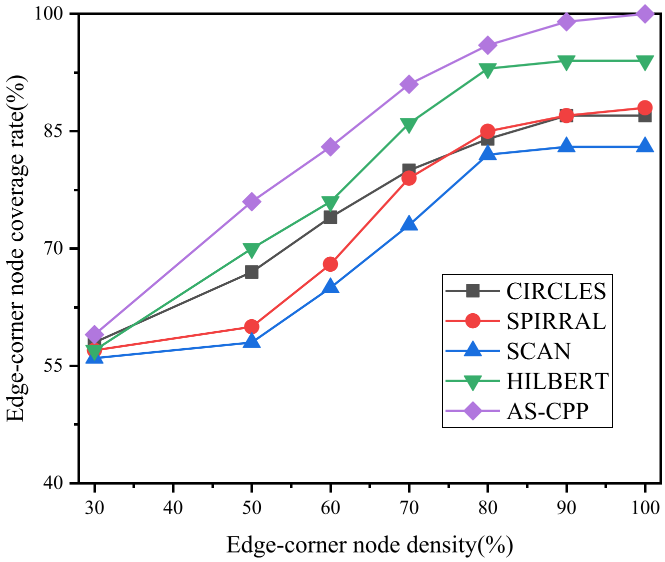

Figure 12. Comparison of edge-corner coverage rates with varying edge-corner node densities.

Table 3. Edge coverage rates with 140 nodes.

Algorithm	Edge-corner coverage
SCAN	86%
HILBERT	90%
SPIRAL	87%
CIRCLES	87%
AS-CPP	93%

Figure 11 shows the variation in edge-corner coverage rates of different algorithms as the number of nodes in the task area increases from 80 to 140. The results indicate that as the number of nodes increases, the edge-corner coverage rates for AS-CPP, SCAN, HILBERT, SPIRAL, and CIRCLES all show an upward trend. However, when the number of nodes is held constant, the AS-CPP exhibits a significant advantage in edge-corner coverage rate.

For example, when there are 140 nodes, table 3 provides a detailed overview of the edge-corner coverage rates for different algorithms. As can be seen from table 3, the AS-CPP has a maximum of 93% edge-corner coverage.

Figure 12 presents the trend in edge-corner coverage rates as the proportion of edge-corner nodes grows from 30% to 100%. When the edge-corner node density is relatively low at 30%, the coverage rates for AS-CPP, CIRCLES, SPIRAL, HILBERT, and SCAN are 59%, 58%, 57%, 57%, and 55%, respectively, showing no significant difference among the algorithms. Furthermore, as shown in figure 12, as the density of corner nodes increases, the coverage of these nodes gradually rises and stabilizes once the density reaches 90%. This result indicates that our method can achieve full coverage within a finite path length, thereby further confirming the convergence of the algorithm. It is observed that with an increase in the proportion of edge-corner nodes, the coverage rates for AS-CPP, SCAN, HILBERT, SPIRAL, and CIRCLES all demonstrate an upward trend, which can be explained by the higher edge-corner node density, which consequently raises the probable chance of node coverage. The AS-CPP consistently demonstrates the highest coverage rate, which grows from *59%* to over 95%. This performance surpasses that of SCAN, HILBERT, SPIRAL, and CIRCLES. This advantage can be attributed to the AS-CPPs adaptive adjustment of spiral radius and the degree of 'squaring' based on edge-corner node density, which optimizes path proximity to edge-corner regions and enhances coverage rates. For example, as the edge-corner proportion reaches 80%, AS-CPP and HILBERT demonstrate sustained coverage rates of 96% and 93%, respectively, while SCAN, SPIRAL, and CIRCLES achieve rates of 82%, 85%, and 84%. These results highlight the superior performance of AS-CPP.

Figure 13 shows the changes in edge-corner node coverage with varying path sampling densities between 15% and 40%. All algorithms demonstrate an enhancement in coverage with the increase in sampling density. The AS-CPP consistently demonstrates superior performance compared to other algorithms across a range of sampling densities. At a sampling density of 40%, all algorithms achieve coverage rates above 80%. However, at lower densities, AS-CPP exhibits a markedly superior edge-corner coverage rate. At a sampling density of 15%, AS-CPPs edge-corner coverage can reach 40%, which is 100%, 66%, 150%, and 81% higher than that of SCAN, HILBERT, SPIRAL, and CIRCLES, respectively.

The impact of the AUVs communication radius on edge-corner coverage is evaluated, with the sampling density and task area size held constant. Figure 14 presents a comparison of coverage rates at communication radii of 300 m, 350 m,

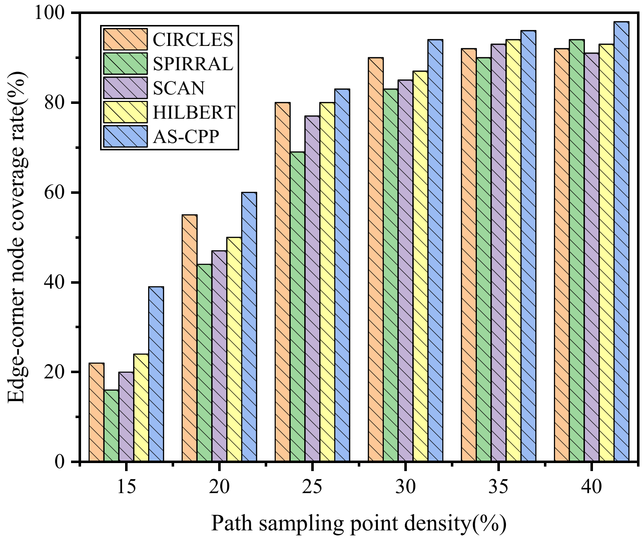

Figure 13. Comparison of edge coverage rates with varying AUV sampling densities.

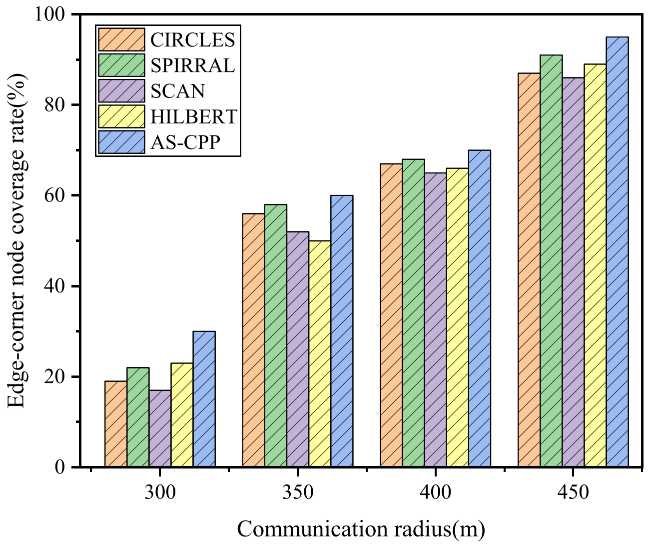

Figure 14. Comparison of edge-corner coverage rates with varying communication radii.

400 m, and 450 m. The results show that an increase in communication radius has a positive effect on edge-corner coverage. Notably, AS-CPP shows significant improvement in edge-corner coverage across varying communication radii. At a lower radius, the advantages of AS-CPP are more pronounced, achieving over 30% coverage at a 300 m radius, compared to 19%, 22%, 17%, and 23% for CIRCLES, SPIRAL, SCAN, and HILBERT, respectively. This is attributed to the fact that AS-CPP is capable of modifying the spiral radius according to the density of edge nodes, thereby reducing the distance between the AUV and the edge-corner areas and consequently improving the coverage.

Table 4. Path length formulas.

Algorithm	Length of path
SPIRAL	$\lambda p\pi\,(2r+pd)+(\lambda-1)\,b$
SCAN	$\lambda\left(4^N-1\right)D_s+(\lambda-1)\,b$
HILBERT	$\frac{L^2}{\lambda}+(\lambda-1)b$
CIRCLES	$2\pi p\sqrt{r^2+\left(\frac{d}{2\pi}\right)^2}$
AS-CPP	$2\pi p\sqrt{\left(r(1-\bar{\rho}^{nor}(1-\frac{r}{L}))\right)^2+\left(\frac{d}{2\pi}\right)^2}$

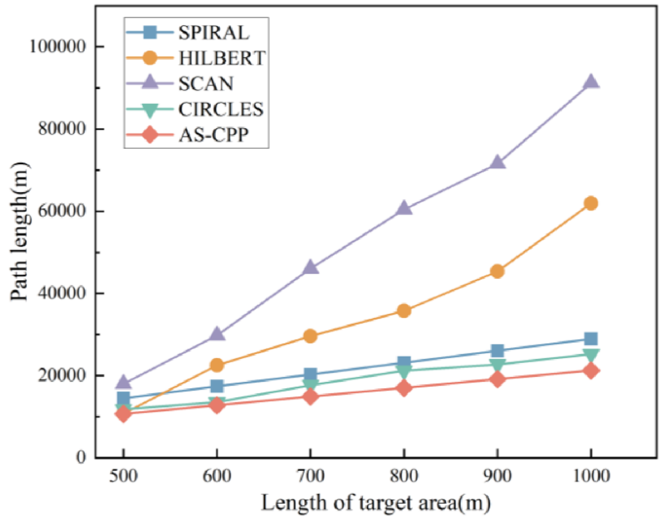

Figure 15. Comparison of algorithm path lengths in different areas.

4.2. Comparison of path lengths and path smoothness for different algorithms

A comparison of the path lengths of four static path planning algorithms was conducted under the same conditions, namely target area size and spatial layering. These were compared with the proposed algorithm using the path length calculation method provided by Han *et al* [34]. The path length formulas are shown in table 4.

In table 4, L is the target area edge length, p is the number of spiral turns, d is the increment per turn, and $\lambda = L/b-1$, $D_s = \frac{L}{2^N}$, where N is the path resolution.

Figure 15 shows the trend of path length changes for the five algorithms under different task area edge lengths, ensuring the same AUV coverage rate. It can be observed from figure 15 that the SCAN algorithm, due to its scanning nature, results in the longest path length and the largest increase. Therefore, the proposed algorithm consistently generates the shortest paths and demonstrates greater robustness, as it is less affected by variations in the target area. This highlights its advantages in maintaining efficient path planning across different environments.

Additionally, when the underwater target area changes, to compare the stability of different path algorithms, the definition of average variation amplitude is proposed:

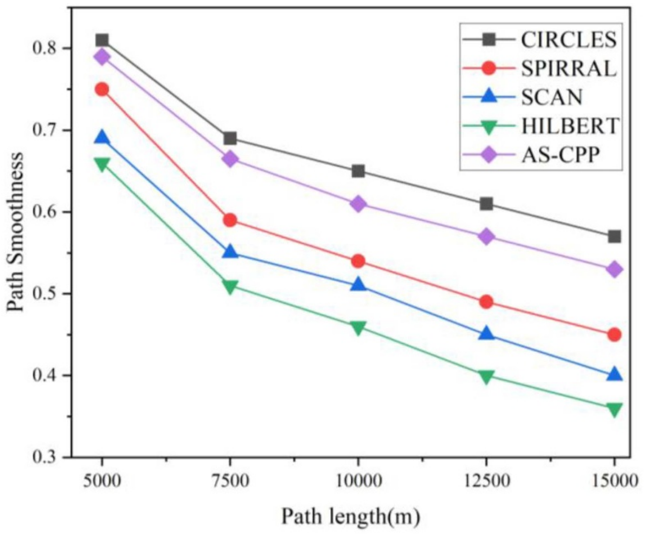

Figure 16. Comparison of path smoothness at different path lengths.

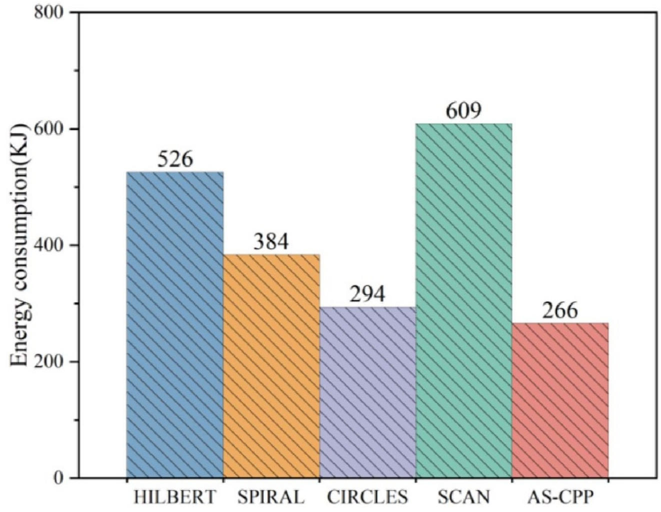

Figure 17. Energy consumption of different path algorithms.

Definition 6: Let the number of target area changes be n, with corresponding path length values Le_0 when unchanged and Le_n after n changes. Then, the path length variation $\hat{r}$ over n changes is expressed as:

$$\hat{r} = \sqrt[n]{\frac{Le_n}{Le_0}} - 1. \tag{43}$$

The proposed AS-CPP achieves shorter paths in comparison to the other algorithms, with a slower growth trend. The variation in path length for n changes is approximately 25%, whereas for the other algorithms it exceeds 50%. The quality of the coverage path is also related to its smoothness. Based on the defined concept of path smoothness and the given calculation formula, we evaluated the path smoothness of SCAN, Hilbert, SPIRAL, CIRCLES, and AS-CPP at different path lengths, as shown in figure 16. It indicates that as path length increases, the smoothness of all five algorithms decreases due to the increased number of turns. However, for the same path length, the CIRCLE path has the best smoothness, followed by AS-CPP, while Hilbert has the worst, aligning with the characteristics of their respective curves.

4.3. Energy consumption comparison across different algorithms

Energy consumption is a key factor in evaluating the efficiency of coverage paths for AUVs. We simulated the energy consumption of an AUV following five different path algorithms under identical conditions, such as movement speed and target area size. The simulation results are shown in figure 17. The energy consumption for the HILBERT, SPIRAL, CIRCLES, SCAN, and the proposed AS-CPP algorithms are 526 KJ, 384 KJ, 294 KJ, 609 KJ, and 266 KJ, respectively. The AS-CPP algorithm has the lowest energy consumption, reducing consumption by 49%, 30%, 9%, and 56% compared to HILBERT, SPIRAL, CIRCLES, and SCAN, respectively. This is because the energy consumption of an AUV is not only related to path length but also to the number and smoothness of turns. The AS-CPP algorithm offers adaptive adjustments, achieving the shortest path length, the fewest turns, and optimal turn smoothness, thereby minimizing energy consumption among these algorithms.

4.4. Localization error and runtime comparison across different algorithms

The quality of a coverage path directly influences localization accuracy in UASNs. We simulated localization errors under different paths, and the results are shown in figure 18. As the AUV's communication range increased from 200 to 600 m, the localization errors for all five algorithms significantly decreased. Under the same localization conditions, the AS-CPP algorithm exhibited higher localization accuracy compared to others. At a communication radius of 600 m, the localization errors for CIRCLES, SPIRAL, and AS-CPP were 0.1419, 0.1272, and 0.1221, respectively. The AS-CPP improved localization accuracy by 13.9% compared to the CIRCLES algorithm and by 4% compared to the SPIRAL algorithm.

Furthermore, the impact of node quantity on localization error was simulated, with node quantities set to 80, 100, 120 and 140. As shown in figure 19, the CIRCLES and AS-CPP algorithms performed better in terms of localization accuracy when the number of nodes was varied. And the AS-CPP algorithm also showed a smaller variation in the localization error curves, and the error reduction rate was calculated to be 5.3%, indicating that the AS-CPP algorithm is more stable and robust.

The computational performance of five CPPs (AS-CPP, CIRCAL, SPIRAL, SCAN, and HILBERT) was evaluated under varying target region sizes. As shown

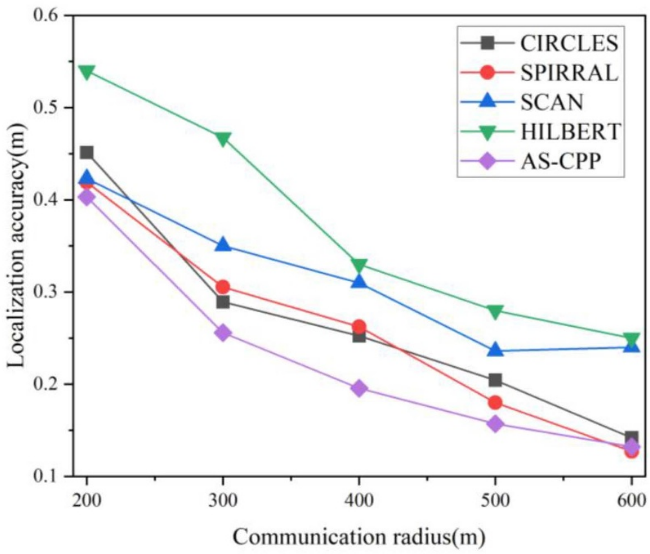

Figure 18. Changes in localization error at different communication radii.

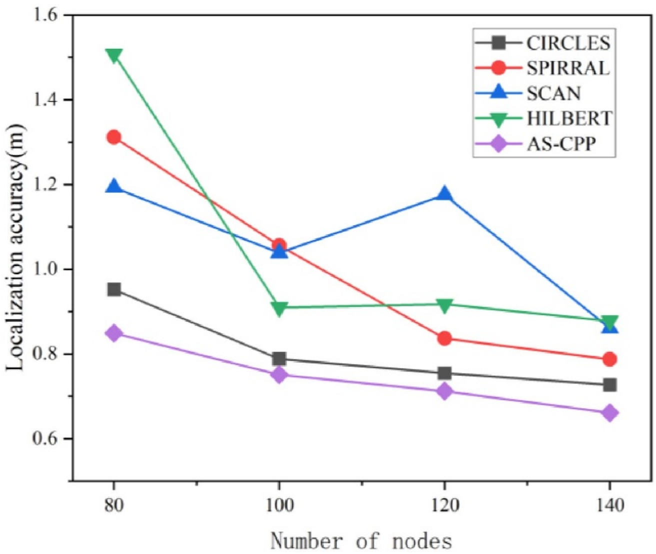

Figure 19. Changes in positioning error with different node quantities.

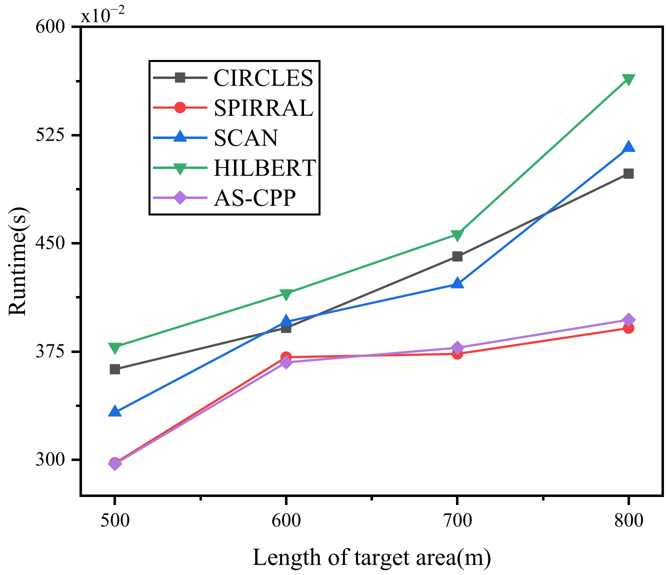

Figure 20. Comparison of algorithm runtime in different areas.

in figure 20, the runtime of different algorithms is compared across target regions with varying side lengths. When the side length of the target area was 500 units, the recorded running times were 2.972×10^{-2} s (AS-CPP), 3.626×10^{-2} s (CIRCAL), 2.977×10^{-2} s (SPIRAL), 3.328×10^{-2} s (SCAN), and 3.784×10^{-2} s (HILBERT). As the region size increased to 600 units, the execution times rose to 3.776×10^{-2} s (AS-CPP), 3.915×10^{-2} s (CIRCAL), 3.733×10^{-2} s (SPIRAL), 3.957×10^{-2} s (SCAN), and 4.152×10^{-2} s (HILBERT). Further expansion to 700 units yielded runtimes of 3.657×10^{-2} s (AS-CPP), 4.409×10^{-2} s (CIRCAL), 3.711×10^{-2} s (SPIRAL), 4.217×10^{-2} s(SCAN), and 4.563×10^{-2} s (HILBERT). Notably, the 800-unit configuration maintained identical timing patterns as the 700-unit scenario. These results demonstrate a positive correlation between target region dimensions and algorithm execution time. Significantly, AS-CPP consistently outperformed SCAN, HILBERT, and CIRCAL across all tested scales, maintaining superior computational efficiency despite increasing problem complexity. This performance advantage highlights AS-CPPs scalability and optimization effectiveness in large-scale coverage path planning scenarios.

5. Conclusion

When an AUV is used as a mobile anchor node within an UASN, the effectiveness of its path planning can significantly impact subsequent node localization. This paper presents an algorithm AS-CPP for 3D target marine environments, particularly addressing scenarios with high node density in edge-corner regions. Based on a 3D spiral model and shape mapping theory, the algorithm controls the degree of 'squaring' and individual layer radii of the path using normalized mean node density values and their respective normalized values per layer. Path performance is evaluated in terms of curvature and smoothness, energy consumption, path length, and edge node coverage. The results of the simulation demonstrate that the AS-CPP path planning scheme exhibits superior performance in comparison to traditional algorithms, including HILBERT, SPIRAL, CIRCLES, and SCAN. It offers a significant improvement in edge-corner coverage, reaching up to 96%, while simultaneously reducing energy consumption by up to 56%. Furthermore, the scheme enhances localization accuracy by up to 13.9%.

In real-world underwater environments, AUVs often face dynamic challenges such as ocean currents and obstacles, which can significantly impact the effectiveness of path planning algorithms. These environmental factors may reduce the efficiency of coverage, particularly in areas with high node density. Furthermore, the performance of the proposed algorithm is also influenced by hardware limitations, including the accuracy of sensors, the communication range, and the processing capacity of the AUVs. Such constraints could affect the algorithm's adaptability and robustness in real-time applications. In the future, we plan to address these challenges by incorporating environmental data, such as ocean currents and moving obstacles, into the path planning process. Additionally, we will explore the potential of multi-AUV coordination to enhance coverage efficiency and provide redundancy in complex scenarios. This will involve improving the algorithm's ability to respond to dynamic conditions while ensuring its scalability.

Data availability statement

All data that support the findings of this study are included within the article (and any supplementary files).

Acknowledgment

Our thanks to the hard-working editors and for valuable comments from the reviewers.

Conflict of interest

The authors declare no conflicts of interest.

Author contributions

Theoretical derivation, simulation test, and writing of the first draft, Z.C. and J.G.; paper revision, X.W.; paper editing, paper review, X.W. and J.M. All authors have read and agreed to the published version of the manuscript.

Funding

This research was sponsored by the National Natural Science Foundation of China (Grant No. 62171179 and No. 61771181).

References

[1] Yan Z and Li Y 2023 Data collection optimization of ocean observation network based on AUV path planning and communication *Ocean Eng.* **282** 114912

[2] Dhongdi S C 2022 Review of underwater mobile sensor network for ocean phenomena monitoring *J. Netw. Comput. Appl.* **205** 103418

[3] Zhou J, Si Y and Chen Y 2023 A review of subsea AUV technology *J. Mar Sci. Eng.* **11** 1119

[4] Wang Q, He B, Zhang Y, Yu F, Huang X and Yang R 2023 An autonomous cooperative system of multi-AUV for underwater targets detection and localization *Eng. Appl. Artif. Intell.* **121** 105907

[5] Cai C, Chen J, Ayub M S and Liu F 2023 A task allocation method for multi-AUV search and rescue with possible target area *J. Mar. Sci. Eng.* **11** 804

[6] Qin H, Zhou N, Han S and Xue Y 2024 An environment information-driven online Bi-level path planning algorithm for underwater search and rescue AUV *Ocean Eng.* **296** 116949

[7] Du J, Han G and Lin C 2024 An autonomous underwater vehicle-assisted adaptive trust prediction model for UASNs *IEEE Trans. Intell. Veh.* 1–10

[8] Gao J, Wang J, Gu J and Shi W 2024 Quantum based deep Q-network bandwidth resource allocation algorithm for UASN *IEEE Internet Things J.* **11** 39932–40

[9] Cheng C, Sha Q, He B and Li G 2021 Path planning and obstacle avoidance for AUV: a review *Ocean Eng.* **235** 109355

[10] Yao P, Qiu L, Qi J and Yang R 2021 AUV path planning for coverage search of static target in ocean environment *Ocean Eng.* **241** 110050

[11] Thilagavathi P Optimizing the static path planning (SPP) methods and path length analysis based on the level sensing resolution of sensor node in wireless sensor network (WSN) *Int. Conf. on Electronics and Sustainable Communication Systems (Coimbatore, India, 2–4 July 2020)* pp 690–6

[12] Mahmoudzadeh S, Powers D M W and Atyabi A 2019 UUV's hierarchical DE-based motion planning in a semi dynamic underwater wireless sensor network *IEEE Trans. Cybern.* **49** 2992–3005

[13] Li M and Zhang H AUV 3D path planning based on A* algorithm *2020 Chinese Automation Congress (CAC) (Shanghai, China, 6–8 November 2020)* pp 11–16

[14] Hao K, Zhao J, Li Z, Liu Y and Zhao L 2022 Dynamic path planning of a three-dimensional underwater AUV based on an adaptive genetic algorithm *Ocean Eng.* **263** 112421

[15] Yan Z, Li J, Wu Y and Zhang G 2019 A real-time path planning algorithm for AUV in unknown underwater environment based on combining PSO and waypoint guidance *Sensors* **19** 20

[16] Li J, Li C, Chen T and Zhang Y 2018 Improved RRT algorithm for AUV target search in unknown 3D environment *J. Mar. Sci. Eng.* **10** 826

[17] Zhu D, Zhou B and Yang S X 2020 A novel algorithm of multi-AUVs task assignment and path planning based on biologically inspired neural network map *IEEE Trans. Intell. Veh.* **6** 333–42

[18] Chu Z, Wang F, Lei T and Luo C 2022 Path planning based on deep reinforcement learning for autonomous underwater vehicles under ocean current disturbance *IEEE Trans. Intell. Veh.* **8** 108–20

[19] Zhang J, Han G, Sha J, Qian Y and Liu J 2021 AUV-assisted subsea exploration method in 6G enabled deep ocean based on a cooperative pac-men mechanism *IEEE Trans. Intell. Transp.* **23** 1649–60

[20] Maki T, Mizushima H, Kondo H, Ura T, Sakamaki T and Yanagisawa M 2007 Real time path-planning of an AUV based on characteristics of passive acoustic landmarks for visual mapping of shallow vent fields OCEANS (29 September 2007–04 October 2007) pp 1–8

[21] Karagol S and Yildiz D 2022 A novel path planning model based on nested regular hexagons for mobile anchor-assisted localization in wireless sensor networks *Arab. J.Sci. Eng.* **47** 9833–48

[22] Salgar M S P 2014 Modified scan algorithm for mobile anchor based localization in wireless sensor network: a brief review *Int. J. Eng. Res. Sci. Technol.* **3** 5

[23] Chen J, Liu X, Wu C, Ma J, Cui Z and Liu Z 2024 An ant colony path planning optimization based on opposition-based learning for AUV in irregular regions *Computing* **106** 2489–520
[24] Fellah K and Kechar B 2020 New approach based on Hilbert curve for energy efficient data collection in WSN with mobile sink *IET Wirel. Sens. Syst.* **10** 214–20
[25] Thilagavathi P and Manickam J M L Circumcenter based mobile beacon aided localization in wireless sensor networks *2023 3rd Int. Conf. on Pervasive Computing and Social Networking (ICPCSN) (Salem, India, 19–20 June 2023)* pp 1107–11
[26] Hu Z, Gu D, Song Z and Li H Localization in wireless sensor networks using a mobile anchor node *2023 3rd Int. Conf. on Pervasive Computing and Social Networking (ICPCSN) (Xi'an, China, 2–5 July 2008)* pp 602–7
[27] Lu Q, Griego A D, Fricke G M and Moses M E Comparing physical and simulated performance of a deterministic and a bio-inspired stochastic foraging strategy for robot swarms *2019 Int. Conf. on Robotics and Automation (ICRA) (Montreal, QC, Canada, 20–24 May 2019)* pp 9285–91
[28] Li L, Li Y, Wang Y, Xu G, Wang H, Gao P and Feng X 2024 Multi-AUV coverage path planning algorithm using side-scan sonar for maritime search *Ocean Eng.* **300** 117396
[29] Mittal K, Song J and Gupta S Real-time motion-planning of curvature-constrained AUVs under steady ocean currents *OCEANS 2019 MTS/IEEE SEATTLE (Seattle, WA, USA, 27–31 October 2019)* pp 1–6
[30] Wang Y, Song S and Liu J Guo X, Cui J 2024 Efficient AUVs-aided localization for large-scale underwater acoustic sensor net-works *IEEE Internet Things J.* **11** 31776–31790
[31] Huang P, Wang Y and Guan X 2024 Information entropy-based trajectory planning for AUV-aided network localization: a reinforcement learning approach *IEEE Internet Things J.* **12** 2122–34
[32] Fong C 2015 2015 Analytical methods for squaring the dis (arXiv:1509.06344)
[33] Underwood A and Murphy C, 2017 Design of a micro-AUV for autonomy development and multi-vehicle systems *OCEANS 2017-Aberdeen* (IEEE) pp 1–6
[34] Han G, Shen S, Song H, Yang T and Zhang W 2018 A stratification-based data collection scheme in underwater acoustic sensor networks *IEEE Trans. Veh. Technol.* **67** 10671–82